

# Absolute/convective instabilities in the Batchelor vortex: a numerical study of the linear impulse response

By IVAN DELBENDE, JEAN-MARC CHOMAZ  
AND PATRICK HUERRE

Laboratoire d'Hydrodynamique, CNRS-UMR 156, École Polytechnique,  
F-91128 Palaiseau Cedex, France

(Received 23 December 1996 and in revised form 14 July 1997)

The absolute/convective instability properties of the Batchelor vortex are determined by direct numerical simulation of the linear impulse response. A novel decomposition procedure is applied to the computed wavepacket in order to retrieve the complex wavenumber and frequency prevailing along each spatio-temporal ray. In particular, the absolute wavenumber and frequency observed in the laboratory frame are determined as a function of swirl parameter and external flow. The introduction of a moderate amount of swirl is found to strongly promote absolute instability. In the case of wakes, the transitional helical mode that first undergoes a switch-over to absolute instability is found to be  $m = -1$  without requiring any external counterflow. In the case of jets, the transitional helical mode is very sensitive to swirl and varies in the range  $-5 \leq m \leq -1$ . Only a slight amount of external counterflow (1.5% of centreline velocity) is then necessary to trigger absolute instability. The results of this numerical procedure are in good qualitative and quantitative agreement with those obtained by direct application of the Briggs–Bers criterion to the inviscid dispersion relation (Olendraru *et al.* 1996). Implications for the dynamics of swirling jets and wakes are discussed.

---

## 1. Introduction

Swirl is known drastically to affect the dynamics of a wide variety of free shear flows such as jets, wakes and mixing layers. The goal of the present study is to demonstrate that axisymmetric jets and wakes experience a transition from convective to absolute instability for moderate swirling levels. Instead of implementing the Briggs–Bers criterion directly on the dispersion relation (see the companion paper, Olendraru *et al.* 1996), we present a novel procedure which relies on a thorough treatment of the linear impulse (or Green) function as determined from direct numerical simulations. The analysis of the large-time asymptotic response leads to the determination of the complex wavenumber and frequency ‘observed’ for each helical mode along distinct spatio-temporal rays. The retrieval of this information is shown to be sufficient to ascertain the convective/absolute nature of the basic flow under consideration. This formulation is illustrated here on the Batchelor vortex which satisfactorily represents the velocity field of trailing line vortices (Batchelor 1964) with superimposed axial flow.

In the absence of any external axial stream, the Batchelor vortex depends on a single non-dimensional parameter, namely the swirl parameter  $q$  which is the ratio of the swirl velocity and axial velocity within the core (see equation (2.2) with  $a = 0$ ). To the present day, most linear instability analyses have been restricted to the temporal framework (real wavenumber, complex frequency). The inviscid instability properties were first examined by Lessen, Singh & Paillet (1974) and more recently by Mayer & Powell (1992). In both instances, the Howard & Gupta (1962) equation was solved numerically in order to determine the dispersion relation between wavenumber and frequency. The main features of inviscid modes may be summarized as follows. When  $q = 0$ , the basic state reduces to a fully developed axisymmetric jet and displays only two unstable helical modes with azimuthal wavenumber  $m = \pm 1$  and identical instability characteristics. Any finite swirl  $q > 0$  leads to the breaking of the reflectional symmetry  $\theta \rightarrow -\theta$ , where  $\theta$  denotes the azimuthal angle. Numerical results indeed indicate that the co-rotating  $m = 1$  mode becomes gradually attenuated. By contrast, as swirl  $q$  is increased, the counter-rotating  $m = -1$  mode is enhanced and higher-order counter-rotating helical modes  $m < -1$  are destabilized. Only modes with  $m < 0$  therefore remain unstable at moderate values of  $q$ . Furthermore, the maximum growth rate over all axial wavenumbers approaches a limiting value as  $m \rightarrow -\infty$  (Leibovich & Stewartson 1983). In this asymptotic régime, the overall maximum growth rate is reached near  $q = 0.87$ . Larger swirl values gradually dampen all helical modes until complete stabilization of the flow for  $q \approx 1.5$ . Similar trends have been observed in the spatial instability (real frequency, complex wavenumber) calculations of Olendraru *et al.* (1996). Corresponding viscous temporal calculations have been performed by Lessen & Paillet (1974), Khorrami (1991) and Mayer & Powell (1992). These investigators have revealed the existence of distinct families of purely viscous modes displaying growth rates that are orders of magnitude below their inviscid counterparts.

These theoretical results have been compared to experimental observations, particularly within the context of vortex breakdown. For extensive discussions on this phenomenon and its manifold theoretical interpretations, the reader is referred to the review articles of Leibovich (1978, 1984), Stuart (1987), Escudier (1988) and Delery (1990), among others. The onset of breakdown in vortices with axial flow is signalled by the appearance of a stagnation point within the core, corresponding to a sudden streamwise deceleration. Time-averaged velocity distributions measured downstream of the stagnation point, in the wake region of the vortex breakdown state, yield  $q$  values below 1.5, which implies that they are temporally unstable (Garg & Leibovich 1979). Furthermore, the observed frequency of the  $m = -1$  instability mode displays good qualitative agreement with the inviscid temporal stability calculations of Lessen *et al.* (1974). Experiments also demonstrate that the velocity distributions measured upstream of the stagnation point, in the jet-like region, correspond to  $q$  values exceeding 1.5, thereby indicating that the incoming flow remains linearly stable (Garg & Leibovich 1979; Escudier, Bornstein & Maxworthy 1982).

Early modelling attempts by Benjamin (1962) have tended to view the occurrence of vortex breakdown as the analogue of hydraulic jumps in supercritical shallow-water layers. In this context, vortices with axial flow can be classified according to the propagating behaviour of the non-dispersive axisymmetric neutral Kelvin waves which they can support in the low-wavenumber limit. Such flows are said to be *supercritical* if they sustain only downstream-travelling waves and *subcritical* if they sustain both upstream and downstream-travelling waves. Vortex breakdown is then

considered as the transition region between an incoming supercritical flow and an outgoing subcritical flow as in a hydraulic jump. This interpretation is supported by the experimental study of Escudier *et al.* (1982): the upstream flow is indeed supercritical and the downstream flow subcritical with respect to low-wavenumber axisymmetric Kelvin disturbances.

These notions have subsequently been extended by Tsai & Widnall (1980) to non-axisymmetric temporal waves of arbitrary real axial wavenumber  $k$ . Whereas Benjamin (1962) used the *phase velocity* at zero wavenumber to discriminate between upstream- and downstream-travelling waves, Tsai & Widnall adopted an *ad-hoc* group velocity criterion based on  $\partial\omega/\partial k$  for neutrally stable waves.† Their analysis, applied to the experimental observations of Garg (1977), indicates that incoming swirling flows exhibiting vortex breakdown are supercritical with respect to helical modes  $m = 0, \pm 1$ . Furthermore, in the case of *axisymmetric* breakdown, the flow displays a transition from supercritical to subcritical with respect to helical modes  $m = 0$  and  $m = +1$ . Finally, in the case of *spiral* vortex breakdown, the supercritical–subcritical transition only occurs for the helical mode  $m = +1$ , the axisymmetric mode  $m = 0$  remaining supercritical throughout.

These ideas can be reinterpreted and generalized by invoking the now widely used concepts of absolute/convective instabilities (see Huerre & Monkewitz 1990 for a review). In this framework, the nature of the instability is determined by examining the linear impulse response of a given basic flow for large time. If the response wavepacket is convected away from the source location, the flow is said to be convectively unstable, i.e. supercritical. If it contaminates the entire medium both upstream and downstream of the source location, the flow is said to be absolutely unstable, i.e. subcritical. The objective of the present study is precisely to determine the absolute/convective nature of the instability in the axial direction for the Batchelor vortex family of swirling flows. In this sense, the investigation constitutes a fully spatio-temporal generalization of the above mentioned analyses.

The linear impulse response of various shear flows has already been examined in the past. The case of the laminar boundary layer on a flat plate was carefully treated both theoretically and experimentally by Gaster (1975) and Gaster & Grant (1975) with excellent agreement between computation and observations in the linear régime. More recently, Park (1990) reconstructed the impulse response wavepacket associated with the asymptotic suction boundary layer on a curved plate subjected to a Görtler instability. In these investigations boundary layers were effectively demonstrated to be convectively unstable with respect to both Tollmien–Schlichting and Görtler instabilities. The corresponding problem for the Kelvin–Helmholtz instability of a piecewise-linear mixing layer has been examined by Balsa (1989).

The paper is organized as follows. The two-parameter family of Batchelor vortices used as basic flows is defined in §2 together with the specification of the governing linearized Navier–Stokes equations and associated initial conditions. The numerical method is outlined in §3. In §4, we describe the local modal decomposition method used to retrieve the large-time asymptotics along each spatio-temporal ray. The absolute/convective nature of the instability is then deduced and mapped in the space of swirl and external flow parameters for each helical mode (§5). The main results and their implications in the vortex breakdown context are presented in a final section §6.

† Phase and group velocities coincide in the low-wavenumber régime where waves become non-dispersive and neutral.

## 2. Problem formulation

A cylindrical coordinate system is adopted, whereby  $x$ ,  $r$  and  $\theta$  respectively denote axial (streamwise) distance, radial distance and azimuthal angle. The basic flow under consideration is chosen to be the steady Batchelor (1964) vortex which, in terms of dimensional variables indicated by a star superscript, admits the axial, radial and azimuthal velocity components

$$U^*(r^*) = U_\infty + (U_c - U_\infty)e^{-(r^*/R)^2}, \quad V^*(r^*) = 0, \quad W^*(r^*) = \Omega_c R \frac{1 - e^{-(r^*/R)^2}}{r^*/R}. \quad (2.1)$$

In the above expressions,  $U_c$  is the centreline axial velocity,  $U_\infty$  is the free-stream axial velocity,  $\Omega_c$  is the rotation rate on the axis and  $R$  is a measure of the core size. Since the basic velocity field is independent of  $x$ , viscous diffusion is assumed to be effectively compensated by a body force, as in all previous instability analyses of the Batchelor vortex. It is convenient to introduce non-dimensional variables (without a star superscript) by selecting as length scale the core size  $R$  and as velocity scale the velocity difference  $\Delta U \equiv U_c - U_\infty$ . In terms of these variables, the basic velocity components (2.1) become

$$U(r) = a + e^{-r^2}, \quad V(r) = 0, \quad W(r) = q \frac{1 - e^{-r^2}}{r}, \quad (2.2)$$

where

$$a \equiv \frac{U_\infty}{\Delta U} \quad \text{and} \quad q \equiv \frac{\Omega_c R}{\Delta U} \quad (2.3)$$

respectively designate the external flow and swirl parameters. The swirl parameter  $q$  is a non-dimensional measure of the core rotation rate whereas the external flow parameter  $a$  is a measure of the free-stream axial velocity far from the axis. When  $q = 0$ , one recovers a fully developed jet or wake velocity profile in the absence of rotation.

Typical axial and azimuthal velocity distributions are displayed on figure 1. The effect of varying the external flow parameter  $a$  is illustrated on figure 1(a,b,c). Coflowing jets correspond to  $a > 0$  (figure 1a), counterflowing jets or wakes to  $-1 < a < 0$  (figure 1b), coflowing wakes to  $a < -1$  (figure 1c).†

Throughout the study, we consider the evolution of infinitesimal disturbances superimposed on the basic flow profiles (2.2) and governed by the non-dimensional linearized incompressible Navier–Stokes equations for the perturbation velocity  $\mathbf{u}(\mathbf{x}, t)$ , pressure  $p(\mathbf{x}, t)$  and vorticity  $\boldsymbol{\omega} = \nabla \times \mathbf{u}$ :

$$\nabla \cdot \mathbf{u} = 0, \quad (2.4)$$

$$\frac{\partial \mathbf{u}}{\partial t} = \mathbf{u} \times \boldsymbol{\Omega} + \mathbf{U} \times \boldsymbol{\omega} - \nabla [p + \mathbf{u} \cdot \mathbf{U}] + \frac{1}{Re} \nabla^2 \mathbf{u}. \quad (2.5)$$

In the above expressions  $\mathbf{U}(r)$  denotes the basic velocity field specified in (2.2) and  $\boldsymbol{\Omega}(r) = \nabla \times \mathbf{U}$  the basic vorticity. The Reynolds number  $Re$  is defined as

$$Re = \frac{\Delta U R}{\nu}, \quad (2.6)$$

where  $\nu$  designates the kinematic viscosity. The viscous diffusion term  $Re^{-1} \nabla^2 \mathbf{U}$  acting on the basic flow has been removed by an effective body force as mentioned previously.

† For wake flows the streamwise direction points towards negative  $x$ .

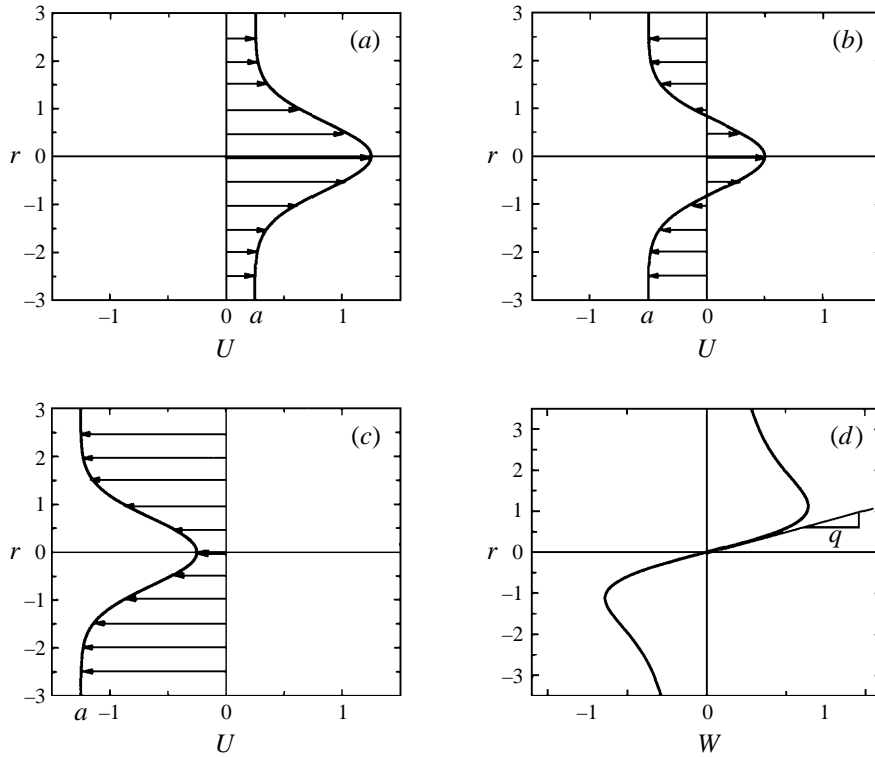


FIGURE 1. Axial velocity profiles: (a)  $a > 0$  coflowing jet, (b)  $-1 < a < 0$  counterflowing wake/jet, (c)  $a < -1$  coflowing wake. (d) Azimuthal velocity profile.

In order to mimic a delta-function forcing in space and time, the following initial conditions are imposed on the perturbations:

$$\begin{pmatrix} u_x \\ u_y \\ u_z \end{pmatrix} = \frac{v_0}{\rho_0} \begin{pmatrix} -(y - y_0) - (z - z_0) \\ x - x_0 \\ x - x_0 \end{pmatrix} \exp \left[ - \left( \frac{\mathbf{x} - \mathbf{x}_0}{\rho_0} \right)^2 \right], \quad (2.7)$$

where, for convenience, we have adopted the usual Cartesian coordinate system  $(x, y, z)$  and associated velocity components  $(u_x, u_y, u_z)$ . Such a velocity distribution satisfactorily represents a localized perturbation of characteristic velocity  $v_0$  concentrated around  $\mathbf{x}_0$  within a sphere of radius  $\rho_0$ . This functional form has been chosen so as to enforce the continuity equation (2.4). The objective of the study is then to analyse the spatio-temporal evolution of the impulse response wavepacket induced by this localized source field. In all that follows, the radial location of the source is chosen to be at  $r_0 = 0.75$ , close to the maximum of the azimuthal vorticity where the jet shear layer is expected to be the most receptive. The other initial condition parameters were chosen to be  $\rho_0 = 0.3$  and  $v_0 = 0.1$ . The selected value of  $\rho_0$  is somewhat of a compromise solution. It should be small enough so that the initial conditions mimic a localized impulse, but it should extend over a few grid points in order to avoid the Gibbs phenomenon arising from spectral truncation.

### 3. Numerical method

Equations (2.4)–(2.5) are effectively solved in Cartesian coordinates within a rectangular box periodically replicated in the three  $x$  (streamwise)-,  $y$ - and  $z$ -directions. A pseudo-spectral scheme has been implemented to integrate numerically this system subject to initial conditions (2.7). The code was originally written by Vincent & Meneguzzi (1991) and adapted to jet instability studies by Brancher, Chomaz & Huerre (1994) and Brancher (1996). The main steps of the numerical method are outlined below.

Let us introduce the usual Fourier transform

$$\hat{\mathbf{u}}(\mathbf{k}, t) = \int \mathbf{u}(\mathbf{x}, t) e^{-i\mathbf{k}\cdot\mathbf{x}} d\mathbf{x} \quad (3.1)$$

whereby the governing equations are transformed into

$$\hat{\mathbf{u}}(\mathbf{k}, t) \cdot \mathbf{k} = 0, \quad (3.2)$$

$$\frac{\partial \hat{\mathbf{u}}}{\partial t}(\mathbf{k}, t) = \mathbf{P}(\mathbf{k})[\mathbf{u} \times \widehat{\boldsymbol{\Omega}} + \mathbf{U} \times \boldsymbol{\omega}](\mathbf{k}, t) - \frac{1}{Re} \mathbf{k}^2 \hat{\mathbf{u}}(\mathbf{k}, t). \quad (3.3)$$

The tensor  $\mathbf{P}(\mathbf{k})$  with Cartesian components  $P_{ij} \equiv \delta_{ij} - k_i k_j / k^2$  designates the projection operator on the space of divergence-free fields.

Time integration between  $t = n\delta t$  and  $t = (n+1)\delta t$  is performed in spectral space via the second-order finite-difference Adams–Bashforth numerical scheme

$$\hat{\mathbf{u}}^{n+1}(\mathbf{k}) = \hat{\mathbf{u}}^n(\mathbf{k}) e^{-k^2 \delta t / Re} + \left( \frac{3}{2} \mathbf{P}^n(\mathbf{k}) e^{-k^2 \delta t / Re} - \frac{1}{2} \mathbf{P}^{n-1}(\mathbf{k}) e^{-2k^2 \delta t / Re} \right) \delta t \quad (3.4)$$

so that the viscous diffusion term in (3.3) is integrated exactly. In equation (3.4),  $\hat{\mathbf{u}}^n(\mathbf{k})$  stands for  $\hat{\mathbf{u}}(\mathbf{k}, n\delta t)$  and  $\mathbf{P}^n(\mathbf{k})$  for  $\mathbf{P}(\mathbf{k})[\mathbf{u}^n \times \widehat{\boldsymbol{\Omega}} + \mathbf{U} \times \boldsymbol{\omega}^n](\mathbf{k})$ . At each time step  $t = n\delta t$  the Fourier transform defined in (3.1) is evaluated. The transform  $\mathbf{u}^n \times \widehat{\boldsymbol{\Omega}} + \mathbf{U} \times \boldsymbol{\omega}^n$  of cross-terms is then calculated and projected via the operator  $\mathbf{P}(\mathbf{k})$ , thereby providing the data necessary to perform the temporal integration to the next time step  $t = (n+1)\delta t$ .

In all simulations, the periodic rectangular box is made up of  $N_x \times N_y \times N_z$  collocation points where  $N_x = 768$  and  $N_y = N_z = 96$ , equally spaced on a Cartesian mesh with  $\delta x = \delta y = \delta z = 0.15$ . The streamwise ( $L_x$ ) and cross-stream ( $L_y = L_z$ ) extent of the box therefore correspond to 115 and 14 jet radii respectively. Such an elongated box is necessary in order to avoid any spurious effects associated with the streamwise-periodic boundary conditions. Streamwise periodicity has indeed been checked to have no significant influence on the wavepacket evolution over the total selected integration time. In spite of the fact that the basic azimuthal velocity  $W(r)$  decays only algebraically fast as  $r \rightarrow \infty$ , the cross-stream periodicity does not introduce any undesirable effects: all computed quantities appearing in (3.3) are linear in the perturbation quantities and therefore decay exponentially when  $r \rightarrow \infty$ , as for all linearized eigenfunctions. A typical exponential decay is of the form  $e^{-kr}$  and it is sufficiently fast provided that the axial wavenumbers of interest are reasonably large: in most situations, these will satisfy the condition  $k > 0.6$  which, for the selected box size, ensures that  $e^{-kr} < 10^{-2}$  at the cross-stream boundaries. Finally, the time increment is chosen to be  $\delta t = 0.01$ , in such a way that the Courant condition  $\delta t < \delta x / U^{\max}$  is fulfilled, where  $U^{\max}$  is the maximum basic velocity. Throughout the study, the Reynolds number has been fixed at  $Re = 667$ , so that the associated grid and time steps lead to reasonable computational size and integration time (6h 40 of CPU time on a Cray 90 for a 3200 iteration run). As expected, lowering  $Re$  causes a

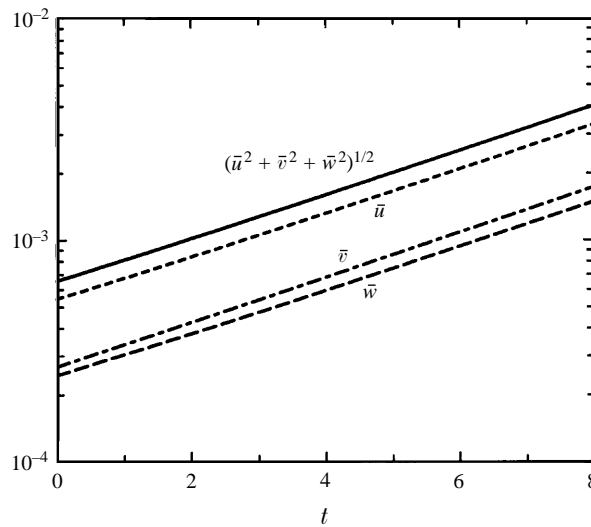


FIGURE 2. DNS code validation for  $a = 0$ ,  $q = 0.4$ ,  $Re = 667$ : temporal evolution of the root-mean-square perturbation velocity  $(\bar{u}^2 + \bar{v}^2 + \bar{w}^2)^{1/2}$  and velocity components  $(\bar{u}, \bar{v}, \bar{w})$ . Initial conditions are chosen to coincide with the  $m = -2$  inviscid eigenmode at  $k = k^{\max} = 0.9$ .

global damping of the solution. However, this effect has not been investigated here, as it does not qualitatively affect the present results.

In order to validate the numerical code, a standard test simulation has been performed as in Brancher *et al.* (1994). Direct numerical simulations initialized by a linearized eigenmode distribution have been compared with the predictions of inviscid linear instability theory. A sample result is shown on figure 2, for a swirling jet at  $a = 0$ ,  $q = 0.4$  and  $Re = 667$ . The initial conditions have been chosen to coincide with the linearized eigenfunction of the (most amplified)  $m = -2$  mode of axial wavenumber  $k = k^{\max} = 0.9$ . The streamwise period of the computational box is therefore selected to be  $L_x = 2\pi/k^{\max}$ . The figure displays the computed temporal evolution of the r.m.s. axial ( $\bar{u}$ ), radial ( $\bar{v}$ ) and azimuthal ( $\bar{w}$ ) perturbation velocity components as well as the r.m.s. perturbation velocity  $(\bar{u}^2 + \bar{v}^2 + \bar{w}^2)^{1/2}$ . Except at the very beginning of the simulation where a slight viscous smoothing takes place, these field variables increase exponentially with the growth rate  $\omega_i = 0.23$ , a result which agrees satisfactorily with the inviscid theoretical value 0.26 if one bears in mind the damping effect of viscosity.

#### 4. Wavepacket response and modal decomposition

Typical calculated impulse responses are displayed in figures 3 and 4 for a non-rotating jet ( $q = 0$ ) and a rotating jet ( $q \neq 0$ ) respectively. Isocontours of streamwise perturbation velocity have been represented to characterize the spatial distribution of the wavepacket. At this level of description, it is impossible to determine unambiguously the leading and trailing edges of the wavepacket: their location naturally depends on the perturbation level selected for the isosurfaces. It is therefore premature to draw any conclusion regarding the absolute or convective nature of the instability. However, such snapshot pictures provide valuable information on the spatial structure and modal content of the impulse response. In the non-rotating case (figure 3), the jet response is dominated by the superposition of counter-rotating helical modes  $m = \pm 1$

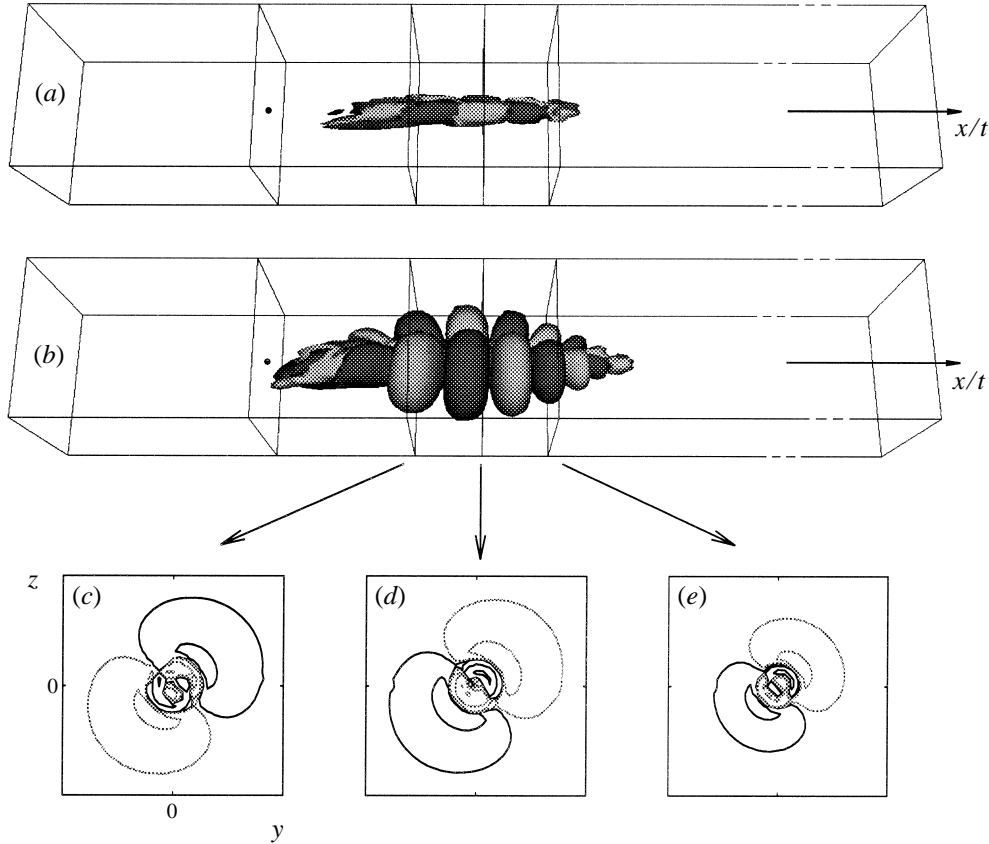


FIGURE 3. Wavepacket spatial distribution at  $t = 32$  for a non-rotating jet at  $a = 0$ ,  $q = 0$ ,  $Re = 667$ . Isosurfaces of axial perturbation velocity component  $u$ : (a)  $u = \pm u^{\max}/20$  and (b)  $u = \pm u^{\max}/1000$ , where  $u^{\max}$  is the maximum value of  $u$  in the entire domain. Isocontours of axial perturbation velocity component  $u$  at various cross-sections corresponding to distinct  $x/t$  stations: (c) at the wavepacket trailing edge  $x/t = 0.4$  for  $u = \pm 10^{-4,-5,-6}$ ; (d) at the wavepacket maximum  $x/t = 0.6$  for  $u = \pm 10^{-3,-4,-5,-6}$ ; (e) at the wavepacket leading edge  $x/t = 0.8$  for  $u = \pm 10^{-4,-5,-6}$ . In these plots, dark regions or lines correspond to positive values of  $u$ , grey regions or lines to negative values of  $u$ .

of equal intensity. The azimuthal standing wave patterns in the various cross-sections  $x/t = \text{const}$  corroborate this observation. This feature is consistent with the fact that the only unstable modes are precisely  $m = \pm 1$ . In the swirling case (figure 4), the impulse response is composed of helical waves which rotate in a direction opposite to that of the basic flow. According to the cross-sectional views (figure 4c,d,e), the azimuthal structure is complex and made up of a superposition of various helical modes of unknown wavenumber  $m$ .

The goal of the following two subsections is to apply appropriate decomposition procedures to the computed impulse response in order to retrieve the temporal instability characteristics for all real wavenumbers (§4.1) and more importantly the long-time asymptotics of the wavepacket (§4.2). In essence, all the observable features of the dispersion relation will be reconstructed from the knowledge of the impulse response. The steps common to these two procedures are outlined below for the axial perturbation velocity component  $u(x, y, z, t)$  generated by DNS.

It is first necessary to compute the velocity  $u(x, r, \theta, t)$  at the nodes of a grid in



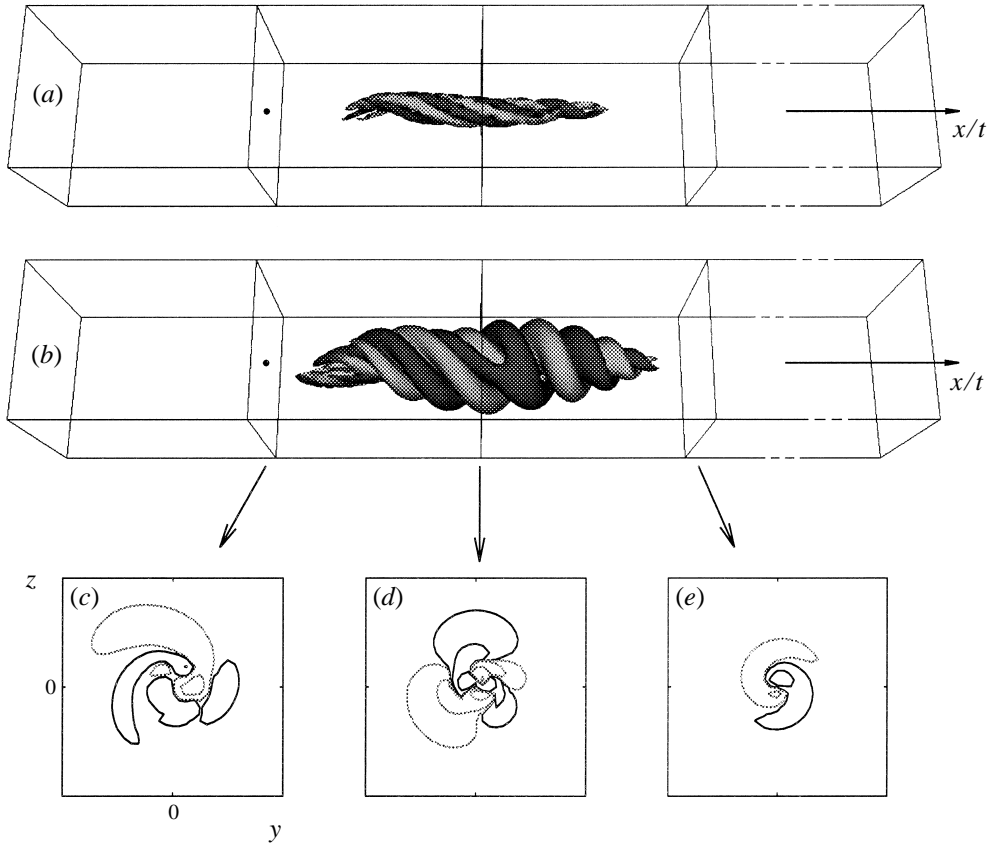


FIGURE 4. (a, b) As figure 3 but for a rotating jet at  $q = 0.4$ , and (c) at the wavepacket trailing-edge near  $x/t = 0$  for  $u = \pm 10^{-5,-6}$ ; (d) at the wavepacket maximum  $x/t = 0.6$  for  $u = \pm 10^{-1,-2,-3}$ ; (e) at the wavepacket leading-edge  $x/t = 0.12$  for  $u = \pm 10^{-5,-6}$ .

the cylindrical coordinate system  $(x, r, \theta)$ . Let  $\hat{u}_{\kappa lp}(t)$  denote the discrete Cartesian Fourier transform with wavenumber indices  $\kappa$ ,  $l$  and  $p$  in the  $x$ -,  $y$ - and  $z$ -directions respectively as generated by DNS. The velocity  $u(x, r, \theta, t)$  at each collocation point is then obtained via the 'slow' reverse Fourier transform

$$u(x, r, \theta, t) = \frac{1}{N_x N_y N_z} \sum_{\kappa lp} \hat{u}_{\kappa lp}(t) \exp 2i\pi \left( \kappa \frac{x}{L_x} + l \frac{r \cos \theta}{L_y} + p \frac{r \sin \theta}{L_z} \right) \quad (4.1)$$

over all Cartesian Fourier modes  $\kappa = -N_x/2, \dots, N_x/2 - 1$ ,  $l = -N_y/2, \dots, N_y/2 - 1$ ,  $p = -N_z/2, \dots, N_z/2 - 1$ .

To define the amplitude and phase of the wavepacket unambiguously, the analytical axial velocity  $\tilde{u}(x, r, \theta, t)$  is introduced through the convolution

$$\tilde{u}(x, r, \theta, t) = \left[ \delta(x) + \frac{i}{\pi x} \right] * u(x, r, \theta, t) \quad (4.2)$$

where symbol  $*$  designates the convolution operator with respect to  $x$ . Conversely  $u(x, r, \theta, t) = \text{Re } \tilde{u}(x, r, \theta, t)$ . In Fourier space, this amounts to setting all negative  $k$ -modes of  $u(x, r, \theta, t)$  to zero in order to recover the usual complex exponential representation.

Finally, each azimuthal component  $m$  is isolated by means of the azimuthal Fourier

transform

$$\tilde{u}_m(x, r, t) = \int_0^{2\pi} \tilde{u}(x, r, \theta, t) e^{-im\theta} d\theta. \quad (4.3)$$

The above steps are implemented on a cylindrical grid with 768 points in the streamwise direction, 20 points in the radial direction and 32 points in the azimuthal direction. The azimuthal wavenumber is therefore restricted to the range  $|m| < 16$ .

#### 4.1. Temporal instability properties

As in Brancher (1996), the broad nature of the wavenumber spectrum defining the initially localized perturbation can effectively be used to extract the temporal history of each individual axial Fourier component  $k$  and to deduce its asymptotic temporal growth rate.

The axial Fourier transform of  $\tilde{u}_m(x, r, t)$  reads

$$\hat{u}_m(k, r, t) = \int_{-\infty}^{+\infty} \tilde{u}_m(x, r, t) e^{-ikx} dx. \quad (4.4)$$

A measure  $\hat{a}_m(k, t)$  of the real amplitude of each Fourier component pair  $(k, m)$  is then

$$\hat{a}_m(k, t) = \left( \int_0^{+\infty} |\hat{u}_m(k, r, t)|^2 r dr \right)^{1/2}. \quad (4.5)$$

A measure  $\varphi_m(k, t)$  of the associated phase distribution at the radial source location  $r_0$  may conveniently be chosen as

$$\varphi_m(k, t) = \arg \hat{u}_m(k, r_0, t), \quad 0 \leq \varphi_m(k, t) < 2\pi. \quad (4.6)$$

The temporal growth rate  $\omega_{m,i}(k)$  can then be obtained through the formula

$$\omega_{m,i}(k) \sim \frac{\partial}{\partial t} \ln \hat{a}_m(k, t), \quad t \rightarrow \infty, \quad (4.7)$$

while the real part  $\omega_{m,r}(k)$  of the frequency is calculated according to the definition

$$\omega_{m,r}(k) \sim -\frac{\partial}{\partial t} \varphi_m(k, t), \quad t \rightarrow \infty. \quad (4.8)$$

In the numerical implementation of this procedure, the logarithmic derivative (4.7) is effectively taken to be

$$\omega_{m,i}(k) \approx \frac{\ln [\hat{a}_m(k, t_2)/\hat{a}_m(k, t_1)]}{t_2 - t_1}, \quad (4.9)$$

where  $t_1 = 16$  and  $t_2 = 32$ , while the derivative (4.8) is evaluated as

$$\omega_{m,r}(k) \approx -\frac{\varphi_m(k, t_3) - \varphi_m(k, t_2)}{t_3 - t_2}, \quad (4.10)$$

where  $t_3 = 32.5$ . Note that the phase function  $\varphi_m(k, t)$  defined in (4.6) is discontinuous whenever it reaches the value 0 or  $2\pi$ . In order to circumvent this difficulty, the time interval  $t_3 - t_2$  appearing in (4.10) is deliberately selected to be much shorter than  $t_2 - t_1$  in (4.9).

Overall results obtained via this procedure are displayed on figure 5 for the Batchelor vortex without external flow  $a = 0$ ,  $q = 0.8$ ,  $Re = 667$ . For this parameter setting, only the first twelve counter-rotating helical modes ( $-12 \leq m \leq -1$ ) are seen to be unstable. The most amplified disturbance is generated at  $m = -4$  and

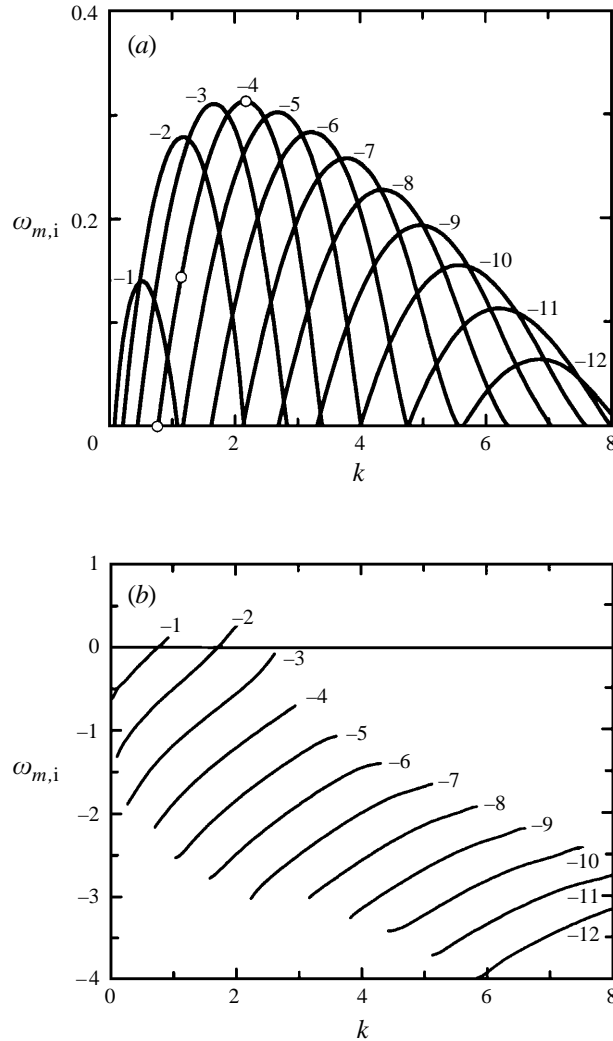


FIGURE 5. Dominant temporal instability modes for  $a = 0$ ,  $q = 0.8$  and  $Re = 667$  retrieved by DNS for each helical mode  $-12 \leq m \leq -1$ : (a) temporal growth rate  $\omega_{m,i}(k)$ ; (b) real part of the frequency  $\omega_{m,r}(k)$ .

$k_{-4}^{\max} = 2.15$ . The axisymmetric mode ( $m = 0$ ), as well as all co-rotating helical modes ( $m > 0$ ) are found to be stable. These results are in qualitative agreement with the linear instability analysis of Lessen *et al.* (1974) summarized in the introduction. According to the latter investigation, higher-order helical modes remain inviscidly unstable for large  $|m|$ ,  $m < 0$ , whereas viscosity is seen to stabilize all modes beyond  $m = -12$  when  $Re = 667$ .

A quantitative comparison between the viscous temporal (VT) instability properties retrieved in such a way and the inviscid temporal (IT) results of Lessen *et al.* (1974) is presented in table 1 for the first six counter-rotating helical modes. The most amplified axial wavenumbers  $k_m^{\max}$  are in excellent agreement. As expected from a fully viscous calculation, associated temporal growth rates  $\omega_{m,i}^{\max}$  are systematically lower than their inviscid counterparts.

---

$m$	$k_m^{\max}$			$\omega_{m,i}^{\max}$		
	IT	VT	WA	IT	VT	WA
-1	0.61	0.54	0.56	0.17	0.14	0.13
-2	1.22	1.18	1.15	0.31	0.27	0.25
-3	1.66	1.68	1.64	0.36	0.31	0.28
-4	2.14	2.17	2.13	0.37	0.31	0.28
-5	2.65	2.68	2.64	0.39	0.30	0.27
-6	3.20	3.22	3.17	0.40	0.28	0.25

---

TABLE 1. Most amplified wavenumber  $k_m^{\max}$  and associated growth rate  $\omega_{m,i}^{\max}$  for the Batchelor vortex without external flow at  $a = 0$ ,  $q = 0.8$ ,  $-6 \leq m \leq -1$ . IT: inviscid temporal instability calculations of Lessen *et al.* (1974); VT: viscous temporal instability properties retrieved by DNS as described in §4.1 for  $Re = 667$ ; WA: wavepacket asymptotics retrieved by DNS as described in §4.2 for  $Re = 667$ .

---

In order to verify that (4.9) leads to reliable estimates of the asymptotic temporal growth rate, it appears essential to check that the radial shape of the corresponding eigenfunction is approximately invariant with time, as shown on figure 6 for different axial wavenumbers at  $m = -4$ : for the most amplified wavenumber  $k_{-4}^{\max} = 2.15$ , the radial distributions  $|\hat{u}_m(k, r, t)|$  and  $\arg \hat{u}_m(k, r, t)$  of amplitude and phase at  $t_1$  and  $t_2$  are indeed invariant (figure 6a). As the wavenumber is lowered to  $k = 1.15$  and  $k = 0.75$  to reach neutral stability (figure 6b,c), the shape invariance gradually deteriorates and remains enforced only near the axis  $r = 0$  over a limited radial extent. For these selected values of  $t_1$  and  $t_2$ , quantitatively accurate results are therefore obtained only sufficiently far away from neutral whence transient effects have become negligible. In order to confirm the accuracy of the results near neutral, one would have to extend the computations over longer integration times and therefore longer axial distances.

#### 4.2. Large-time wavepacket asymptotics

The objective of the following procedure is to determine the complex streamwise wavenumber  $k_m(v_g)$  and complex frequency  $\omega_m(v_g)$  observed along each spatio-temporal ray  $x/t = v_g$  for different azimuthal modes  $m$  in the asymptotic régime  $t \rightarrow \infty$ . This is usually achieved analytically by resorting to steepest-descent arguments (Bers 1983), according to which each azimuthal mode is expected to evolve as

$$\tilde{u}_m(x, r, t) \sim F_m(v_g, r, t) e^{i[k_m(v_g)x - \omega_m(v_g)t]}, \quad t \rightarrow \infty. \quad (4.11)$$

In the above expression  $F_m(v_g, r, t)$  is an algebraically decaying function of time that involves the eigenfunction pertaining to  $k_m$ .

In what follows, it will prove useful to introduce the growth rate  $\sigma_m(v_g)$  ‘observed’ along a particular spatio-temporal ray  $x/t = v_g$  for the azimuthal mode  $m$ . According to (4.11),

$$\sigma_m(v_g) = \omega_{m,i}(v_g) - k_{m,i}(v_g)v_g. \quad (4.12)$$

Let

$$A_m(x, t) = \left( \int_0^{+\infty} |\tilde{u}_m(x, r, t)|^2 r \, dr \right)^{1/2} \quad (4.13)$$

denote the real amplitude pertaining to azimuthal mode  $m$ , and

$$\Phi_m(x, t) = \arg \tilde{u}_m(x, r_0, t), \quad 0 \leq \Phi_m(k, t) < 2\pi, \quad (4.14)$$

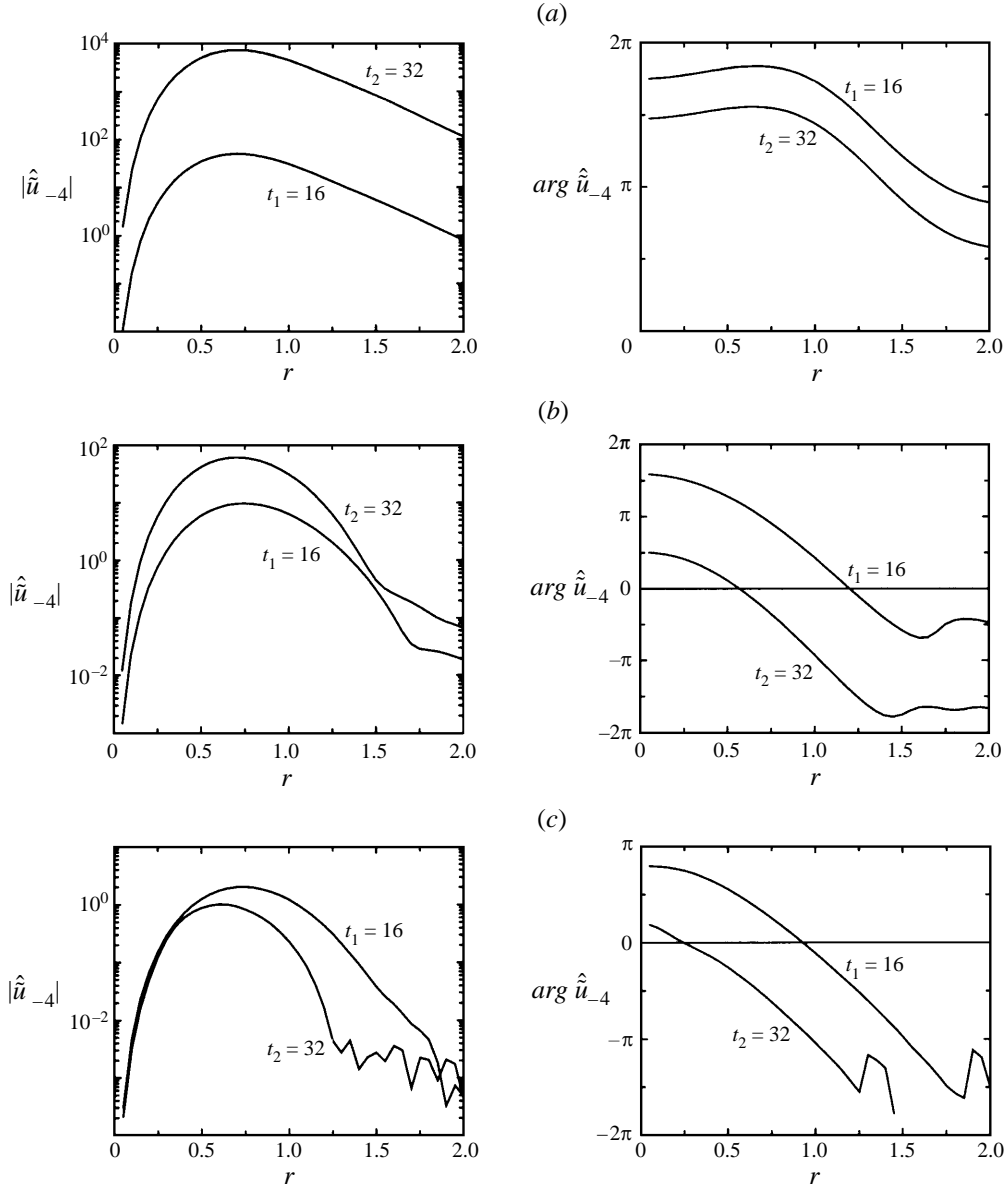


FIGURE 6. Radial distribution of temporal eigenfunction  $\hat{u}_m(r, k, t)$  for azimuthal mode  $m = -4$  retrieved by DNS from the perturbation axial velocity fields at  $t_1 = 16$  and  $t_2 = 32$  with  $a = 0$ ,  $q = 0.8$ ,  $Re = 667$ . The amplitude (left) is represented on a semi-log plot and the phase (right) on a linear plot at three values of the axial wavenumber  $k$  indicated by the symbols  $\circ$  on figure 5(a): (a)  $k = k_{-4}^{\max} = 2.15$ , (b)  $k = 1.15$  and (c) near neutral  $k = 0.75$ .

the associated phase function measured at the radial source location  $r_0$ . It is now possible to retrieve from (4.13)–(4.14) all the characteristics  $k_m(v_g)$ ,  $\omega_m(v_g)$  and  $\sigma_m(v_g)$  along  $x/t = v_g$ , as defined in (4.11)–(4.12).

The temporal growth rate  $\sigma_m(v_g)$  is given by

$$\sigma_m(v_g) \sim \frac{d}{dt} \ln A_m(v_g t, t), \quad t \rightarrow \infty. \quad (4.15)$$

As demonstrated in the Appendix, the imaginary part  $k_{m,i}$  of the wavenumber ‘observed’ along  $x/t = v_g$  is simply given by

$$-k_{m,i}(v_g) = \frac{d\sigma_m}{dv_g}(v_g), \quad (4.16)$$

where it is implied that  $v_g$  is real. Knowing  $\sigma_m(v_g)$  and  $k_{m,i}(v_g)$ , the corresponding imaginary part  $\omega_{m,i}$  of the frequency is calculated from (4.12) according to the formula

$$\omega_{m,i}(v_g) = \sigma_m(v_g) + k_{m,i}(v_g)v_g. \quad (4.17)$$

By definition, the real parts of  $k_m(v_g)$  and  $\omega_m(v_g)$  are related to the phase function  $\Phi_m(x, t)$  defined in (4.14) via the expressions

$$k_{m,r}(v_g) \sim \frac{\partial}{\partial x} \Phi_m(x = v_g t, t), \quad t \rightarrow \infty, \quad (4.18)$$

and

$$\omega_{m,r}(v_g) \sim -\frac{\partial}{\partial t} \Phi_m(x = v_g t, t), \quad t \rightarrow \infty. \quad (4.19)$$

Thus the quantities  $\sigma_m$ ,  $-k_{m,i}$ ,  $\omega_{m,i}$ ,  $k_{m,r}$  and  $\omega_{m,r}$  may all be determined as a function of  $v_g$  by making use of expressions (4.15)–(4.19).

In the numerical evaluation of these functions, the logarithmic derivative appearing in (4.15) is taken to be

$$\sigma_m(v_g) \approx \frac{\ln[A_m(v_g t_2, t_2)/A_m(v_g t_1, t_1)]}{t_2 - t_1}, \quad (4.20)$$

with  $t_1 = 16$  and  $t_2 = 32$ . The function  $\sigma_m(v_g)$  is thereby evaluated in the range  $-0.625 \leq v_g \leq 2.972$  in successive steps of size  $\delta v_g = \delta x/t_2 \approx 4.7 \times 10^{-3}$ . Equation (4.16) is discretized into

$$-k_{m,i}(v_g) \approx \frac{\sigma_m(v_g + \delta v_g) - \sigma_m(v_g)}{\delta v_g}, \quad (4.21)$$

with the same step size  $\delta v_g$ . Finally, (4.18) and (4.19) are discretized into

$$k_{m,r}(v_g) \approx \frac{\Phi_m(v_g t_2 + \delta x, t_2) - \Phi_m(v_g t_2, t_2)}{\delta x}, \quad (4.22)$$

$$\omega_{m,r}(v_g) \approx -\frac{\Phi_m(v_g t_2, t_3) - \Phi_m(v_g t_2, t_2)}{t_3 - t_2}, \quad (4.23)$$

where  $t_3 = 32.5$ . Note that, in the same spirit as in §4.1, the growth rate  $\sigma_m(v_g)$  is estimated over the large time increment  $t_2 - t_1$  (equation (4.20)). By contrast,  $\omega_{m,r}(v_g)$  is evaluated over the small time increment  $t_3 - t_2$  (equation (4.23)) in order to account for possible phase discontinuities.

The above methodology leads to a complete determination of the wavepacket characteristics along each spatio-temporal ray  $x/t = v_g$ . A typical amplitude distribution of the various helical modes  $A_m(x, t)$  is illustrated on figure 7(a) for the Batchelor vortex without external flow. The associated growth rates  $\sigma_m(v_g)$  are displayed on figure 7(b), as a function of group velocity  $x/t = v_g$ .

The impulse response is seen to be composed of individual wavepackets pertaining to different azimuthal modes  $m$ . The curves  $\sigma_m(v_g)$  contain all the essential information necessary to characterize the spatio-temporal behaviour of each azimuthal mode. As sketched on figure 8, the streamwise extent of each wavepacket is delineated by rays

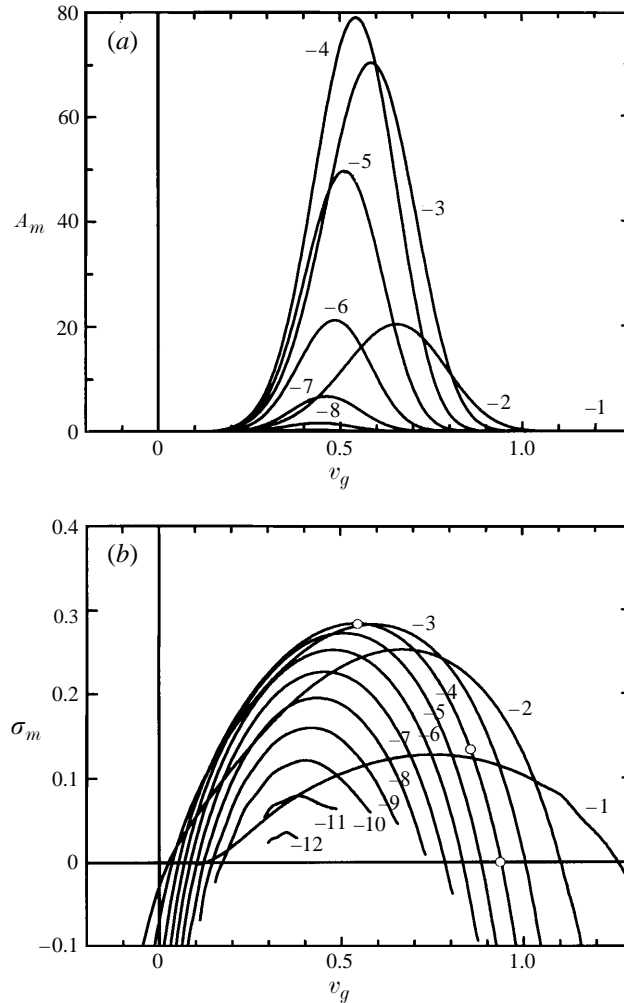


FIGURE 7. (a) Amplitude distribution  $A_m(x, t)$  of dominant azimuthal modes  $-8 \leq m \leq -1$  at  $t = 32$  for  $a = 0$ ,  $q = 0.8$  and  $Re = 667$ . Linear scale. (b) Corresponding growth rate  $\sigma_m(v_g)$  'observed' along each spatio-temporal ray  $x/t = v_g$  for  $-12 \leq m \leq -1$ .

$v_{g,m}^+$  and  $v_{g,m}^-$  such that  $\sigma_m(v_g) = 0$  and along which a neutral wave is observed. To each helical mode  $m$ , one may associate an absolute growth rate  $\omega_{0,m,i}$  observed in the laboratory frame, i.e. along the ray  $x/t = v_g = 0$ . The quantity  $\omega_{0,m,i}$  therefore coincides with  $\sigma_m(0)$ , as illustrated on figure 8.

Let  $v_{g,m}^{\max} \equiv \partial \omega_{m,i} / \partial k(k_m^{\max})$  denote the spatio-temporal ray along which one observes the most amplified wavenumber  $k_m^{\max}$  over all real axial wavenumbers, such that  $\partial \omega_{m,i} / \partial k(k_m^{\max}) = 0$ . Since  $k_{m,i}^{\max} = 0$ , (4.12) reduces to  $\sigma_m = \omega_{m,i}^{\max}$  and (4.16) yields  $d\sigma_m/dv_g(v_{g,m}^{\max}) = 0$ . It can therefore be concluded that  $\omega_{m,i}^{\max}$  is also the maximum growth rate over all ray directions  $x/t = v_g$ , as sketched on figure 8. The associated group velocity  $v_{g,m}^{\max}$  is therefore a measure of the velocity of the wavepacket of azimuthal mode  $m$ .

It is straightforward to extend these definitions to the full impulse response: its streamwise extent is delineated by the fastest leading edge  $v_g^+$  and the slowest trailing edge  $v_g^-$ , which may pertain to distinct helical modes  $m$ . Its overall absolute growth

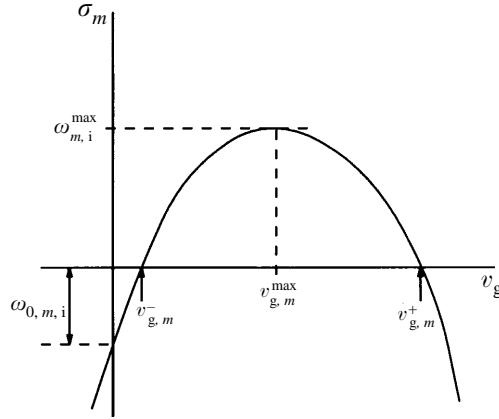


FIGURE 8. Characteristic quantities pertaining to the growth rate curve  $\sigma_m(v_g)$  for the wavepacket of azimuthal wavenumber  $m$ . The curve displays a maximum at the ray velocity  $v_{g,m}^{\max}$  whence  $\sigma_m(v_{g,m}^{\max}) = \omega_{m,i}^{\max}$ . Leading- and trailing-edge  $v_{g,m}^{\pm}$  velocities correspond to  $\sigma_m(v_g) = 0$ . The absolute growth rate  $\omega_{0,m,i}$  coincides with  $\sigma_m(0)$ .

rate  $\omega_{0,i}$  is the maximum absolute growth rate over all  $m$ . If it is positive (negative), the flow is absolutely (convectively) unstable.

For the parameter setting  $a = 0$ ,  $q = 0.8$  and  $Re = 667$ , the leading and trailing edges of the full wavepacket are associated with azimuthal modes  $m = -1$  and  $m = -2$  respectively (figure 7b) and they propagate with velocities  $v_g^+$  and  $v_g^-$  that are both positive. As a result, the overall absolute growth rate  $\omega_{0,i}$  is negative and the flow is convectively unstable.

In table 1, the maximum growth rate  $\omega_{m,i}^{\max}$  over all ray directions  $v_g$  obtained from the above wavepacket asymptotics (WA) is compared with its viscous temporal (VT) counterpart over all real wavenumbers  $k$ , as calculated in §4.1: these theoretically identical quantities as well as the associated wavenumbers  $k_m^{\max}$  are seen to coincide within 10% accuracy.

The above wavepacket decomposition has been applied to the DNS-generated impulse response of the Batchelor vortex without external flow at  $a = 0$ ,  $Re = 667$  and  $q = 0, 0.1, 0.2, 0.4, 0.5, 0.6, 0.7, 0.8, 0.9, 1, 1.2, 1.3, 1.4, 1.5$ . For all swirl values, the leading- and trailing-edge velocities  $v_g^+$  and  $v_g^-$  are found to be both positive as in figure 7(b). One may therefore conclude that the zero-external-flow Batchelor vortex is at most convectively unstable for  $Re = 667$ .

Although the curves  $\sigma_m(v_g)$  are sufficient to determine the absolute/convective nature of the instability, a complete specification of the wavepacket asymptotic behaviour requires the calculation of the complex frequency  $\omega_m(v_g)$  and wavenumber  $k_m(v_g)$  as given in (4.16)–(4.19). Corresponding results are displayed on figure 9 for the same parameter values as in figure 7. Smooth variations of  $k_m$  and  $\omega_m$  are obtained at all but the lowest azimuthal wavenumbers. Spurious oscillations are observed at  $m = -12$  and  $m = -11$ : the energy levels are then so small that there is contamination by the more energetic azimuthal modes. Note also the presence of a bump near  $v_g = 1.1$  in the curves relative to  $m = -1$ . This feature is possibly due to a shift in the most amplified mode at  $m = -1$ , as  $v_g$  is increased.

In the same spirit as in §4.1, it may be checked that for the selected times  $t_1 = 16$  and  $t_2 = 32$ , radial distributions are shape-invariant along each spatio-temporal ray  $x/t = v_g$ . Sample validation results are displayed on figure 10 for three particular



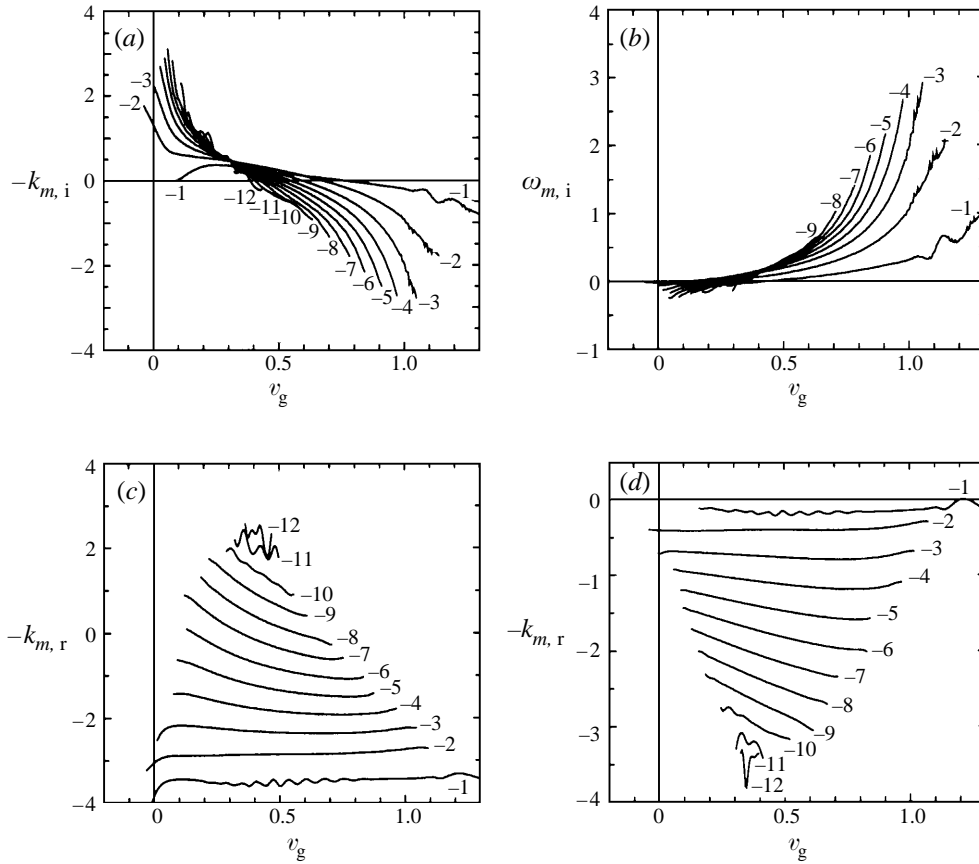


FIGURE 9. Distribution of (a)  $-k_{m,i}(v_g)$ , (b)  $\omega_{m,i}(v_g)$ , (c)  $k_{m,r}(v_g)$  and (d)  $\omega_{m,r}(v_g)$  relative to azimuthal modes  $-12 \leq m \leq -1$  at  $t = 32$  for  $a = 0$ ,  $q = 0.8$  and  $Re = 667$ .

group velocities indicated by open circles on figure 7(b): retrieved axial eigenfunctions are seen to preserve their shape between  $t_1$  and  $t_2$  so that transients have died out and asymptotic formula (4.11) indeed applies.

### 5. Convective/absolute properties of the Batchelor vortex with external flow

An essential feature of the present approach lies in its ability to deduce the absolute/convective nature of the instability for arbitrary values of the external flow parameter  $a$  solely from the results for zero external flow ( $a = 0$ ). We exploit the fact that, at a given value of  $q$ , the impulse response for  $a \neq 0$  may be obtained by applying a trivial Galilean transformation of velocity  $a$  to its zero-external-flow counterpart.

More specifically the Green function  $u(x, r, \theta, t; a)$  for finite external flow  $a$  is related to the Green function  $u(x, r, \theta, t; 0)$  for zero external flow via the change of variable

$$u(x, r, \theta, t; a) = u(x - at, r, \theta, t; 0). \quad (5.1)$$

Note that (5.1) remains applicable for obtaining the response to any initial distribution of perturbations. Equivalently, in terms of the group velocity  $x/t = v_g$ ,

$$u(v_g, r, \theta, t; a) = u(v_g - a, r, \theta, t; 0). \quad (5.2)$$

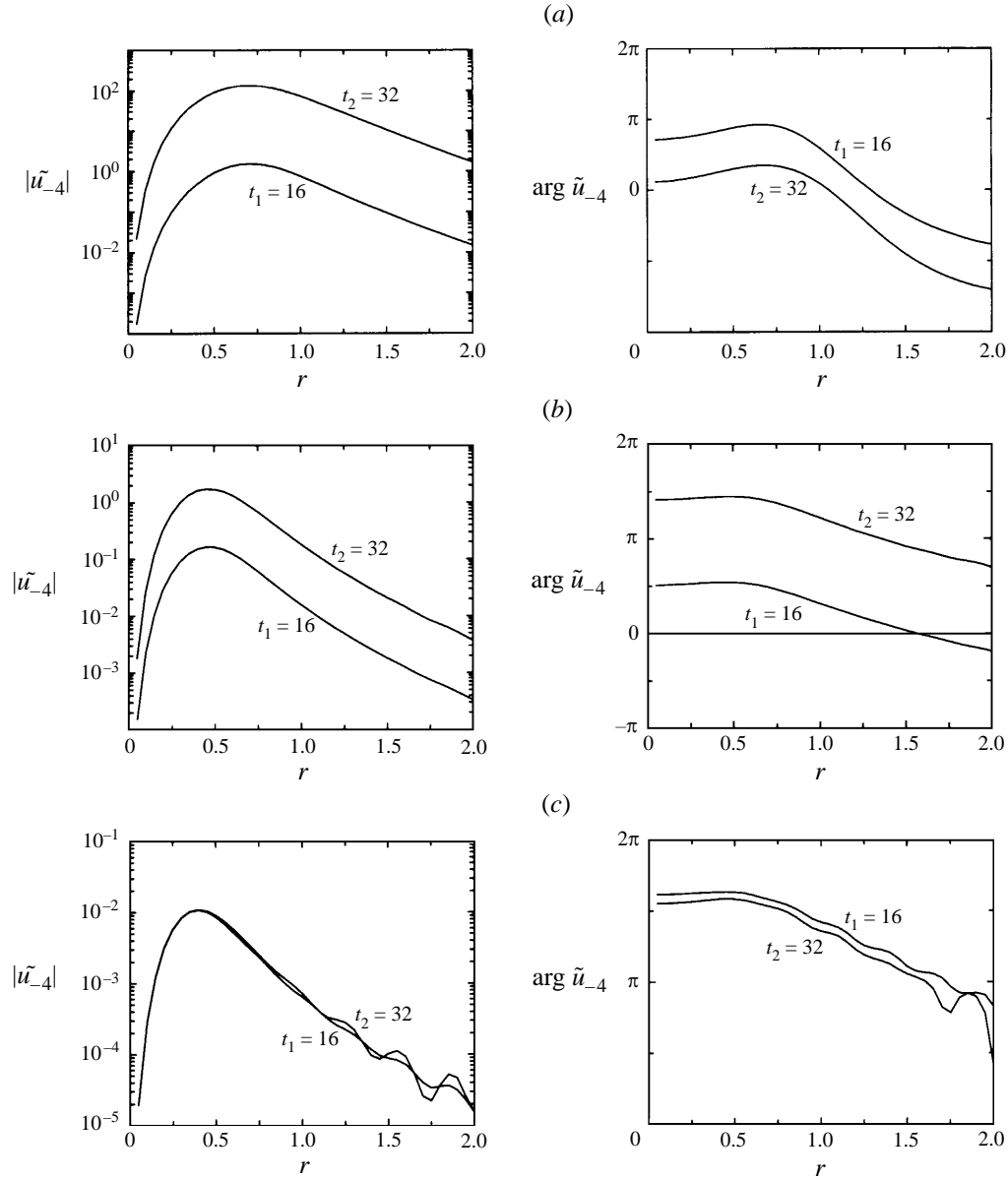


FIGURE 10. Radial distribution of spatio-temporal eigenfunction  $\tilde{u}_m(r, k, t)$  for azimuthal mode  $m = -4$  retrieved by DNS from the perturbation axial velocity fields at  $t_1 = 16$  and  $t_2 = 32$  with  $a = 0$ ,  $q = 0.8$ ,  $Re = 667$ . The amplitude (left) is represented on a semi-log plot and the phase (right) on a linear plot at three values of the group velocity  $v_g$  indicated by the symbols  $\circ$  on figure 7(b): (a)  $v_g = v_{g,-4}^{\max} = 0.55$ , (b)  $v_g = 0.84$  and (c) at the leading-edge  $v_g = v_{g,-4}^+ = 0.94$ .

In the context of expression (4.11), (5.2) implies that the complex wavenumber  $k_m$  and frequency  $\omega_m$  for finite external flow can be deduced from their zero-external-flow analogues through the Doppler shift transformation

$$k_m(v_g; a) = k_m(v_g - a; 0), \quad (5.3)$$

$$\omega_m(v_g; a) = a k_m(v_g - a; 0) + \omega_m(v_g - a; 0). \quad (5.4)$$

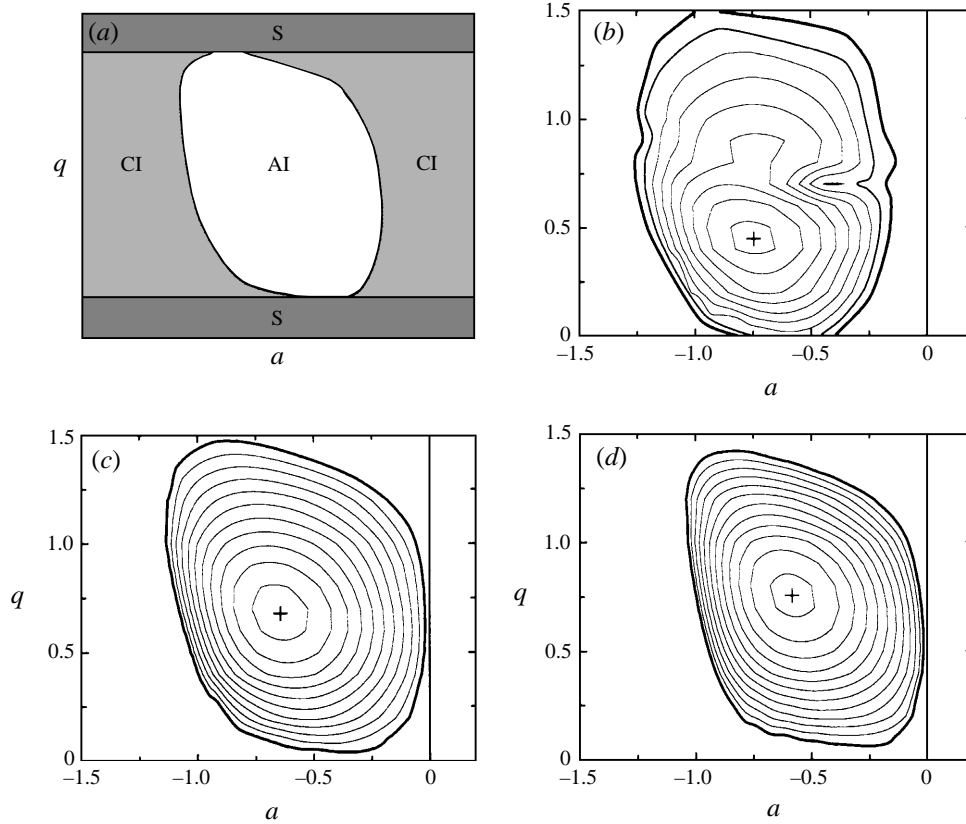


FIGURE 11. (a) Typical instability properties of each azimuthal mode: the absolute instability region (AI) is nested within the convectively unstable zone (CI); outside a horizontal band of finite height in  $q$  the azimuthal mode remains stable (S). (b–d) Isocontours of absolute growth rate  $\omega_{0,m,i}$  in parameter plane  $(a, q)$  for azimuthal modes (b)  $m = -1$ , (c)  $m = -2$  and (d)  $m = -3$ . The bold curve corresponds to  $\omega_{0,m,i} = 0$ . Isocontours of  $\omega_{0,m,i}$  in step increases of 0.025, for positive values only, have been reported in order to delineate clearly the absolute instability region.

As a result, the growth rate  $\sigma_m(v_g; a) = \omega_{m,i}(v_g; a) - k_{m,i}(v_g; a)v_g$  observed along the spatio-temporal ray  $x/t = v_g$  is transformed according to the rule

$$\sigma_m(v_g; a) = \sigma_m(v_g - a; 0). \quad (5.5)$$

The observed growth rate curves of figure 7(b) therefore experience a simple translation of amount  $a$  along the  $v_g$ -axis. The same reasoning may be invoked to obtain finite-external-flow results for all swirl parameter values  $q$  of interest. Thus, for each parameter setting  $(a, q)$ , the diagnostic quantities introduced in §4.2 and sketched in figure 8 may be calculated. In particular the absolute growth rate  $\omega_{0,m,i}$  satisfies  $\omega_{0,m,i} \equiv \sigma_m(0; a) = \sigma_m(-a; 0)$  and it may directly be read off figure 7(b) by setting  $v_g = -a$ . Remaining quantities such as  $k_{0,m,r}$  and  $\omega_{0,m,r}$  may similarly be calculated by applying (5.3) and (5.4).

Resulting isolines of absolute growth rate  $\omega_{0,m,i}$  in the  $(a, q)$ -plane are displayed on figure 11 for azimuthal wavenumbers  $m = -1, -2$  and  $-3$ . As sketched in figure 11(a), the particular contour  $\omega_{0,m,i} = 0$  typically delineates an oval domain within which  $\omega_{0,m,i} > 0$  and mode  $m$  therefore exhibits absolute instability (AI). Outside this region, mode  $m$  is either convectively unstable (CI) or stable (S). The neutral curves

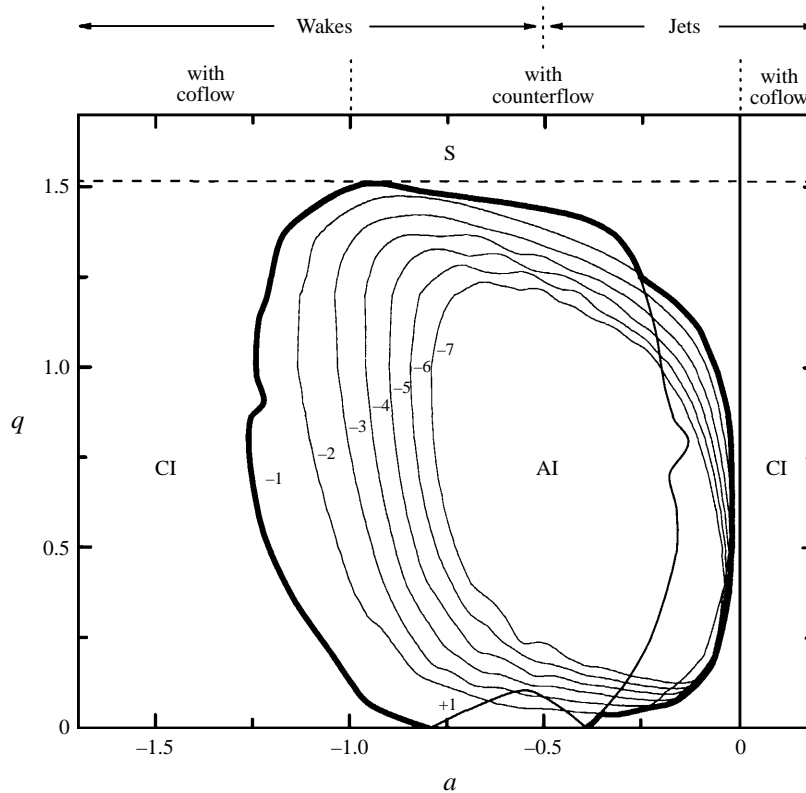


FIGURE 12. Regions of stability (S), convective instability (CI) and absolute instability (AI) in the  $(a, q)$  parameter plane for the Batchelor vortex at  $Re = 667$ . Thin lines indicate AI/CI transition curves for each azimuthal mode  $m = +1$  and  $m = -1, \dots, -7$ . Bold line denotes outermost boundary of AI region.

separating the CI, AI regions from the S region do not depend on the magnitude of the external flow parameter  $a$  and are therefore straight horizontal lines  $q = \text{const}$ . Typically each mode  $m$  becomes unstable in a horizontal band at intermediate values of the swirl parameter  $q$ . Note that  $m = \pm 1$  are the only unstable modes at  $q = 0$ . All other modes are stable at sufficiently low  $q$ . For large swirl values, all modes are ultimately stabilized. These results are entirely consistent with the temporal instability analyses of Lessen *et al.* (1974) and Mayer & Powell (1992) summarized in §1.

The AI region typically lies in the left half-plane  $a < 0$  which implies that negative external flow is a prerequisite for absolute instability. More specifically, for each swirl level  $q$  within the unstable horizontal band, there exists a range of negative external flow values giving rise to AI. As  $q$  is increased from the lower neutral value (from zero in the case  $m = -1$ ), the extent of the AI range gradually widens towards both the zero-external-flow axis and the large negative-external-flow values. The reverse trend is observed as the swirl  $q$  approaches the upper neutral curve. Furthermore the absolute growth rate  $\omega_{0,m,i}$  reaches a well defined maximum within the AI zone at a particular value of  $a$  and  $q$ .

In order to determine the overall instability properties, the various absolute/convective transition curves  $\omega_{0,m,i} = 0$  are overlaid on figure 12 for  $m = +1$  and  $m = -1, \dots, -7$ . The global AI/CI transition boundary is given by the outermost envelope

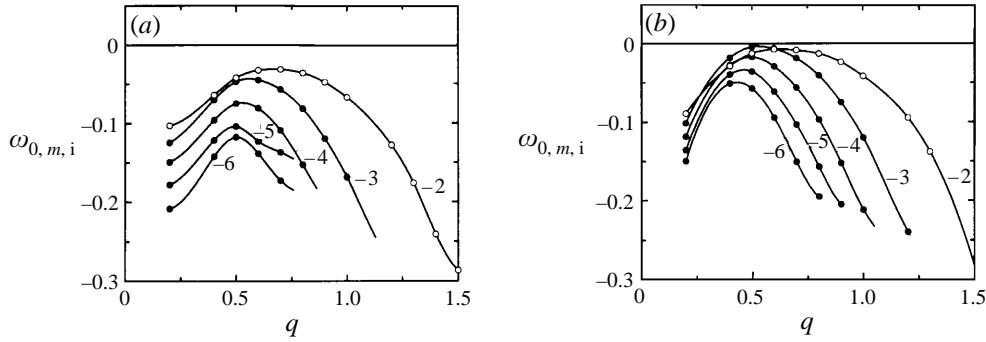


FIGURE 13. Absolute growth rate  $\omega_{0,m,i}$  as a function of  $q$ : (a) without external flow ( $a = 0$ ), and (b) at the minimum counterflow value giving rise to CI/AI transition  $a = -0.014$ .

of the individual transition curves pertaining to different values of  $m$ . If higher-order azimuthal modes  $m \leq -8$  are taken into consideration, corresponding transitional curves  $\omega_{0,m,i} = 0$  become nested one inside the other so that the outer CI/AI boundary remains unaffected.

In the no-swirl case ( $q = 0$ ), absolute instability is triggered by the  $m = \pm 1$  modes and it prevails in the range  $-0.80 < a < -0.39$ , i.e. for wake/jet configurations with sufficiently large counterflow (figure 1b). As  $q$  increases, the AI range widens towards  $a = 0$  (zero-counterflow jet) and  $a = -1$  (zero-counterflow wake).

On the wake side ( $a < -0.5$ ), the transitional mode leading to AI remains  $m = -1$  at all swirl values. It is essential to note that for swirl values as low as 0.13, wakes may undergo a transition to AI for  $a < -1$ , i.e. without requiring any external counterflow.

On the jet side ( $a > -0.5$ ), the transitional mode first leading to AI as  $q$  increases varies in discrete steps from  $m = -1$  to  $m = -2, -3, -4, -5, -4, -3, -2, -1$ . Crossover points from one azimuthal mode to another can only be very coarsely determined on account of the finite 0.1 step size in  $q$ . Furthermore, absolute instability may be triggered for a counterflow as small as  $a = -0.015 \pm 0.001$  provided that swirl is of order  $q = 0.55 \pm 0.05$ . The transitional AI/CI curve runs almost parallel to the  $q$ -axis and only a slight amount of counterflow is therefore necessary to provoke AI onset over an extended range  $0.2 < q < 1$ . Moreover, when  $0.2 < q < 0.5$ , AI/CI transition curves pertaining to  $m = -2, -3, \dots$  remain extremely close to each other. This is further confirmed by the absolute growth rate curves prevailing in the zero-external-flow jet ( $a = 0$ ) and the AI/CI transitional jet ( $a = -0.014$ ) as shown in figure 13. For such small external flows, the value of swirl that is optimum to promote AI is seen to lie in the range  $0.5 < q < 0.7$ . It should be noticed that this range of values of  $q$  does not include the most unstable swirl  $q \approx 0.87$  discussed in the introduction.

The same representation may be used for the real parts of the absolute wavenumber  $k_{0,m,r}$  and absolute frequency  $\omega_{0,m,r}$  resulting from the application of (5.3) and (5.4) at  $v_g = 0$ . Typical results are displayed on figure 14 for azimuthal modes  $m = -1, -2, -3$ . These results may be compared with those obtained in the context of non-rotating axisymmetric bluff body wakes by Monkewitz (1988a) for the family of parallel axial velocity profiles

$$U(r; A, N) = 1 - A + \frac{2A}{1 + (e^{r^2 \ln 2} - 1)^N}. \quad (5.6)$$

In the above equation,  $A$  denotes the velocity ratio  $A = (U_c - U_\infty)/(U_c + U_\infty)$

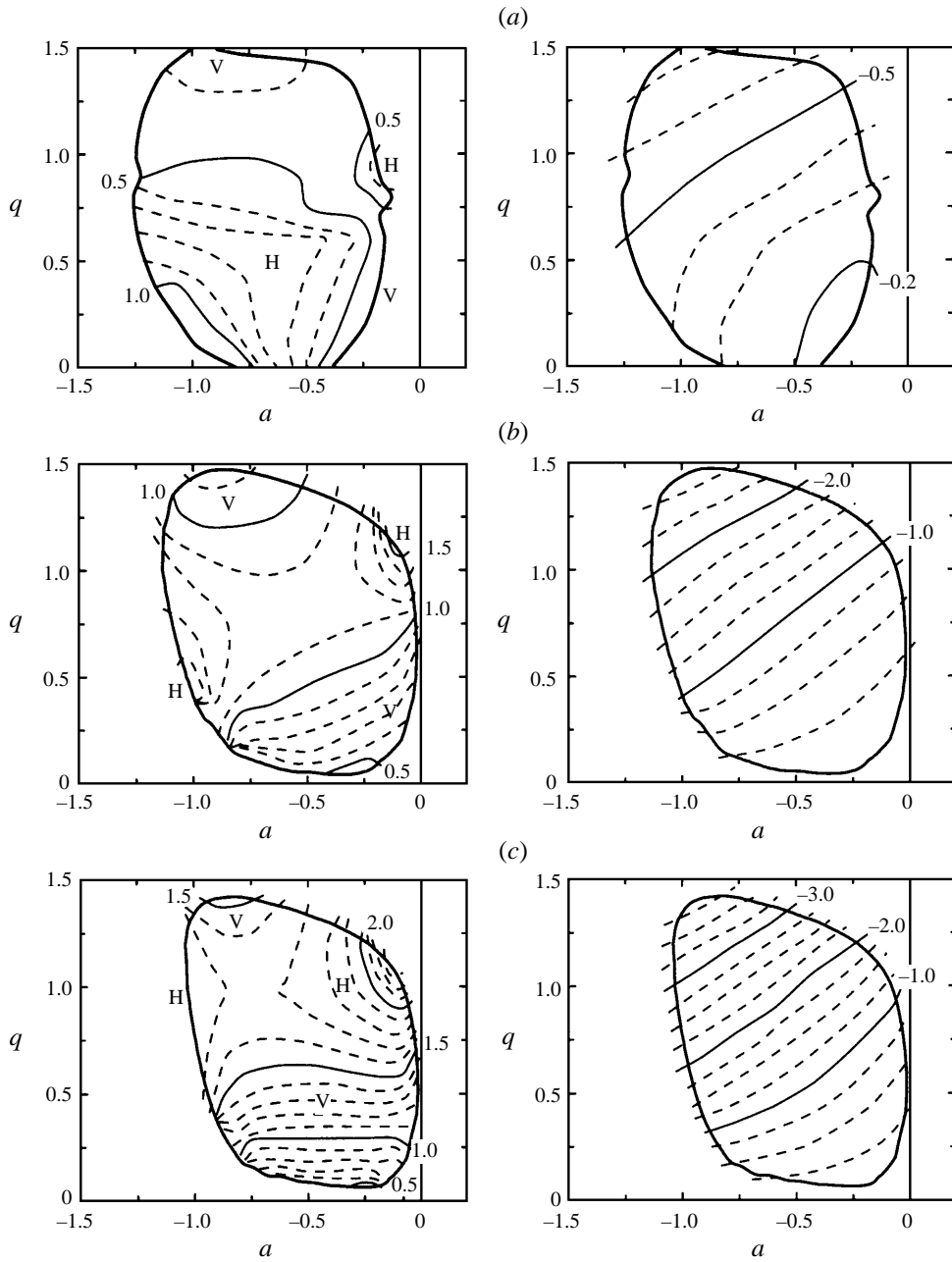


FIGURE 14. Isocontours of real absolute wavenumber  $k_{0,m,r}$  (left) and real absolute frequency  $\omega_{0,m,r}$  (right) in the  $(a, q)$  parameter plane for azimuthal modes (a)  $m = -1$ , (b)  $m = -2$  and (c)  $m = -3$ . The bold curve corresponds to  $\omega_{0,m,i} = 0$ . Isoline values are indicated on each contour plot. H and V denote 'hills' and 'valleys' of saddle points of surface  $k_{0,m,r}$ .

and  $N$  a shape parameter. In the particular case  $N = 1$ , one recovers our zero-swirl basic velocity field provided that  $a = (1 - A)/2A$  and  $q = 0$ . The complex absolute wavenumbers and frequencies  $k_{0,\pm 1}^{(M)}$  and  $\omega_{0,\pm 1}^{(M)}$  calculated by Monkewitz (1988a) for  $m = \pm 1$  at  $Re = \infty$  translate into the present  $k_{0,\pm 1}$  and  $\omega_{0,\pm 1}$  via the scaling relations  $k_{0,\pm 1} = k_{0,\pm 1}^{(M)}/(\ln 2)^{1/2}$  and  $\omega_{0,\pm 1} = \omega_{0,\pm 1}^{(M)}/(4A^2 \ln 2)^{1/2}$ . At  $A = -1$ , i.e.  $a = -1$ , Monkewitz found  $k_{0,\pm 1}^{(M)} = 1.04 - 0.85i$  and  $\omega_{0,\pm 1}^{(M)} = 0.75 - 0.20i$ , i.e.  $k_{0,\pm 1} = 1.25 - 1.02i$  and  $\omega_{0,\pm 1} = -0.45 - 0.12i$ . Extrapolated values from the results displayed in figures 11(b) and 14(a) yield  $k_{0,\pm 1} = 1.20 - 0.73i$  and  $\omega_{0,\pm 1} = -0.39 - 0.06i$ : real parts are in good quantitative agreement whereas imaginary parts noticeably differ on account of their smaller absolute values. Similar trends prevail for corresponding results obtained at  $A = -1.1$ , i.e.  $a \approx -0.95$ .

## 6. Conclusions and discussion

A detailed analysis of the transition from convective to absolute instability has been presented for the Batchelor vortex as a function of external flow  $a$  and swirl  $q$  for a fixed Reynolds number  $Re = 667$ . The application of swirl has been found to widen considerably the range of external flow values giving rise to absolute instability. In wakes ( $a < -0.5$ ), the ‘critical’ helical mode for absolute instability onset is  $m = -1$  and no counterflow is necessary to trigger absolute instability over almost the entire range of unstable  $q$ . In jets ( $a > -0.5$ ), the ‘critical’ helical mode is found to be extremely sensitive to swirl. A slight counterflow  $a \approx -0.015$  equivalent to 1.5% of the centreline axial velocity remains necessary in order to trigger absolute instability. This value is to be compared with  $a = -0.39$  corresponding to 64% of the centreline axial velocity in the absence of swirl.

A new method has been presented in order to retrieve the main features of the dispersion relation from direct numerical simulations of the linear impulse response. This procedure leads to the determination of the dominant complex frequency and wavenumber observed along each spatio-temporal ray  $x/t = v_g$ . In particular, one may calculate the complex absolute frequency and wavenumber and thereby identify domains of absolute and convective instability.

The results of the present investigation have been compared with a direct application of the zero-group-velocity criterion to the inviscid dispersion relation  $D[k, \omega; a, q] = 0$  as performed in Olendraru *et al.* (1996). AI/CI transition curves obtained via each method are overlaid on figure 15. There is good overall qualitative and quantitative agreement over a wide domain in the  $(a, q)$ -plane but the direct numerical simulation procedure yields a slightly smaller region of AI. In particular, the analysis of the inviscid dispersion relation predicts the occurrence of AI/CI transition on the co-flowing jet side  $a > 0$ . By contrast, the fully viscous numerical study of the linear impulse response slightly pushes AI/CI transition into the counterflow side  $a < 0$ .

The merits and disadvantages of the present procedure are as follows. In a single run, the direct simulation of the impulse response provides a global picture of all dominant modes along all spatio-temporal rays  $x/t = v_g$ . However, its successful implementation requires large computational domains in order to avoid end effects, which makes it costly in computer time. In addition, this methodology is incapable of isolating less-unstable modes. For instance, we have not determined the role, if any, played by the purely viscous modes of Khorrami (1991) and Mayer & Powell (1992). It may very well be that their effect is masked by faster growing inviscid-like

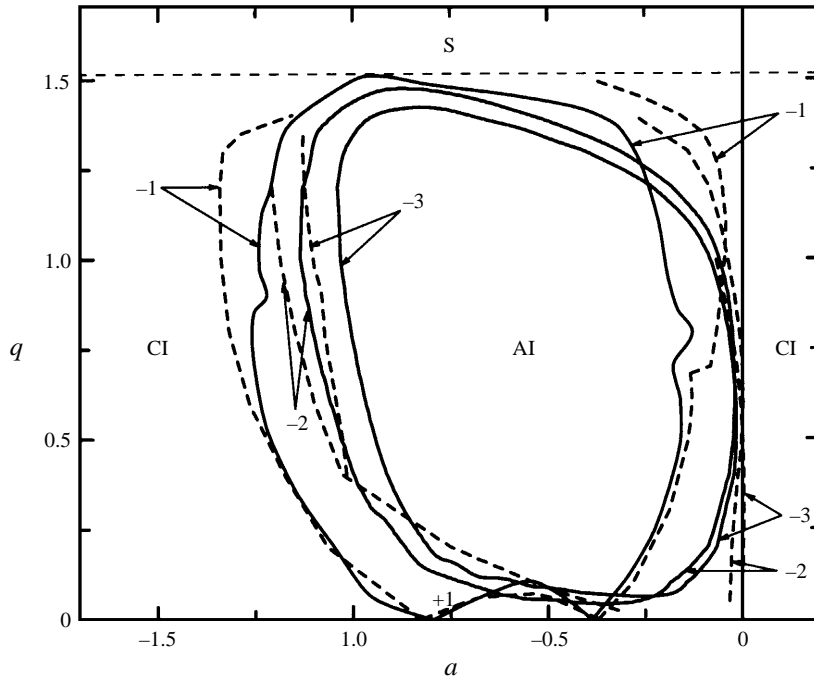


FIGURE 15. AI/CI transition curves in the  $(a, q)$  parameter plane for azimuthal modes  $m = \pm 1, -2, -3$ . Solid lines: present study at  $Re = 667$ . Dashed lines: results of Olendraru *et al.* (1996) obtained by application of the zero-group-velocity criterion to the inviscid dispersion relation of the Batchelor vortex.

modes. It is also important to emphasize that as a result of finite time integration, the method slightly underestimates the spatio-temporal growth rate and therefore the extent of the absolutely unstable region. Although high precision cannot be expected from the present method, the results provide excellent guess values, which considerably facilitates the hunt for pertinent saddle points as required in the Briggs–Bers criterion. More generally the procedure is most useful whenever the dispersion relation cannot be derived explicitly due to the complexity of the basic flow. For instance, it has successfully been applied by Brancher & Chomaz (1997) to the study of secondary instabilities in two-dimensional spatially periodic shear flows.

The presence of a sufficiently large region of absolute instability is known to encourage the onset of synchronized self-sustained oscillations commonly referred to as global modes (Chomaz, Huerre & Redekopp 1988). According to the present investigation, swirl is likely to increase drastically the extent of the absolutely unstable region and thereby the synchronization of spatially developing wakes and jets. For instance, helical vortex shedding behind non-rotating axisymmetric bluff bodies has been ascribed by Monkewitz (1988*a*) to the existence of an absolutely unstable ‘source’ region located in the near wake. Only the first helical mode  $m = \pm 1$  is then found to be absolutely unstable, in agreement with experimental observations. The results of the present investigation suggest that the application of swirl will rapidly single out  $m = -1$  as the dominant helical mode within such wake flows.

It is much more delicate to interpret the occurrence of breakdown in vortices with axial flow in the light of the present results. Experiments indicate that breakdown is either axisymmetric ( $m = 0$ ) or spiral ( $m = -1$ ), whereas in the jet range ( $a > -0.5$ )



our analysis shows higher-order helical modes ( $m = -2, -3, \dots$ ) to be favoured. However, the present results upstream and downstream of the stagnation point might very well prove to be pertinent in accounting for the unsteady behaviour of the observed breakdown states. Garg & Leibovich (1979) have emphasized that ‘vortex breakdown, of either the bubble or spiral form, act like solid objects in changing an upstream jet-like flow into a wake-like flow’. The observed dominant oscillations of the wake then correspond to the counter-rotating spiral mode  $m = -1$ , in agreement with the AI/CI analysis for wakes ( $a < -0.5$ ).

In order to reach a more definite conclusion, one would have to carry out a detailed investigation of the AI/CI nature of measured velocity profiles at each downstream station, as in the wake studies of Monkewitz (1988*a,b*).

The authors acknowledge financial support by the Direction des Recherches, Études et Techniques (DRET) of the French Ministry of Defence under Grant No 92-098, as well as the computational facilities of the Institut du Développement et des Ressources en Informatique Scientifique (IDRIS/CNRS). The authors would like to thank P. Brancher, T. Loiseleux, C. Olendraru and L. Tuckerman for an efficient and stimulating collaboration. Thanks are warmly extended to T. Lescuyer, J. Webert and all the pre-fa-mily for maintaining a friendly and congenial atmosphere.

#### Appendix. Proof of relation (4.16)

Differentiation of (4.12) with respect to  $v_g$  leads to

$$\frac{d\sigma_m}{dv_g} = \frac{d\omega_{m,i}}{dv_g} - \frac{dk_{m,i}}{dv_g} v_g - k_{m,i}. \quad (\text{A } 1)$$

The Cauchy–Riemann conditions imply that

$$v_g \equiv \frac{d\omega_m}{dk} = \frac{\partial\omega_{m,r}}{\partial k_{m,r}} + i \frac{\partial\omega_{m,i}}{\partial k_{m,r}} = \frac{\partial\omega_{m,i}}{\partial k_{m,i}} + i \frac{\partial\omega_{m,i}}{\partial k_{m,r}}. \quad (\text{A } 2)$$

Only real values of the group velocity  $v_g = d\omega_m/dk$  are of interest here, in which case (A 2) reduces to the identities

$$v_g = \frac{\partial\omega_{m,i}}{\partial k_{m,i}} \quad \text{and} \quad \frac{\partial\omega_{m,i}}{\partial k_{m,r}} = 0. \quad (\text{A } 3)$$

Under this real group velocity condition, the chain rule and (A 3) imply that

$$\frac{d\omega_{m,i}}{dv_g} = \frac{\partial\omega_{m,i}}{\partial k_{m,i}} \frac{dk_{m,i}}{dv_g} = v_g \frac{dk_{m,i}}{dv_g}, \quad (\text{A } 4)$$

and (A 1) effectively reduces to relation (4.16).

#### REFERENCES

- BALSA, T. F. 1989 Three-dimensional wave packets and instability waves in free shear layers and their receptivity. *J. Fluid Mech.* **201**, 77–97.
- BATCHELOR, G. K. 1964 Axial flow in trailing line vortices. *J. Fluid Mech.* **20**, 645–658.
- BENJAMIN, T. B. 1962 Theory of the vortex breakdown phenomenon. *J. Fluid Mech.* **14**, 529–551.
- BERS, A. 1983 Space-time evolution of plasma instabilities – absolute and convective. In *Handbook of Plasma Physics* (ed. M. N. Rosenbluth & R. Z. Sagdeev), vol. 1, pp. 451–517. North-Holland.
- BRANCHER, P. 1996 Étude numérique des instabilités secondaires de jets. PhD thesis, École Polytechnique, France.

- BRANCHER, P. & CHOMAZ, J.-M. 1997 Absolute and convective secondary instabilities in spatially periodic shear flows. *Phys. Rev. Lett.* **78**, 658–661.
- BRANCHER, P., CHOMAZ, J.-M. & HUERRE, P. 1994 Direct numerical simulations of round jets: vortex induction and side jets. *Phys. Fluids* **6**, 1768–1774.
- CHOMAZ, J.-M., HUERRE, P. & REDEKOPP, L. G. 1988 Bifurcations to local and global modes in spatially developing flows. *Phys. Rev. Lett.* **60**, 25–29.
- DELERY, J. M. 1990 Aspects of vortex breakdown. *Prog. Aerospace Sci.* **30**, 1–59.
- ESCUDIER, M. P. 1988 Vortex breakdown: observations and explanations. *Prog. Aerospace Sci.* **25**, 189–229.
- ESCUDIER, M. P., BORNSTEIN, J. & MAXWORTHY, T. 1982 The dynamics of confined vortices. *Proc. R. Soc. Lond. A* **382**, 335–360.
- GARG, A. K. 1977 Oscillatory behavior in vortex breakdown flows: an experimental study using a laser anemometer. MS thesis, Cornell University.
- GARG, A. K. & LEIBOVICH, S. 1979 Spectral characteristics of vortex breakdown flowfields. *Phys. Fluids* **22**, 2053–2064.
- GASTER, M. 1975 A theoretical model of a wave packet in the boundary layer on a flat plate. *Proc. R. Soc. Lond. A* **347**, 271–289.
- GASTER, M. & GRANT, I. 1975 An experimental investigation of the formation and development of a wave packet in a laminar boundary layer. *Proc. R. Soc. Lond. A* **347**, 253–269.
- HOWARD, L. N. & GUPTA, A. S. 1962 On the hydrodynamic and hydromagnetic stability of swirling flows. *J. Fluid Mech.* **14**, 463–476.
- HUERRE, P. & MONKEWITZ, P. A. 1990 Local and global instabilities in spatially developing flows. *Ann. Rev. Fluid Mech.* **22**, 473–537.
- KHORRAMI, M. R. 1991 On the viscous modes of instability of a trailing line vortex. *J. Fluid Mech.* **255**, 197–212.
- LEIBOVICH, S. 1978 The structure of vortex breakdown. *Ann. Rev. Fluid Mech.* **10**, 221–246.
- LEIBOVICH, S. 1984 Vortex stability and breakdown: survey and extension. *AIAA J.* **22**, 1192–1206.
- LEIBOVICH, S. & STEWARTSON, K. 1983 A sufficient condition for the instability of columnar vortices. *J. Fluid Mech.* **126**, 335–356.
- LESSEN, M. & PAILLET, F. 1974 The stability of a trailing line vortex. Part 2. Viscous theory. *J. Fluid Mech.* **65**, 769–779.
- LESSEN, M., SINGH, P. J. & PAILLET, F. 1974 The stability of a trailing line vortex. Part 1. Inviscid theory. *J. Fluid Mech.* **63**, 753–763.
- MAYER, E. W. & POWELL, K. G. 1992 Viscous and inviscid instabilities of a trailing line vortex. *J. Fluid Mech.* **245**, 91–114.
- MONKEWITZ, P. A. 1988*a* A note on vortex shedding from axisymmetric bluff bodies. *J. Fluid Mech.* **192**, 561–575.
- MONKEWITZ, P. A. 1988*b* The absolute and convective nature of instability in two-dimensional wakes at low Reynolds numbers. *Phys. Fluids* **31**, 999–1006.
- OLENDRARU, C., SELLIER, A., ROSSI, M. & HUERRE, P. 1996 Absolute/convective instability of the Batchelor vortex. *C. R. Acad. Sci. Paris* **323** (IIb), 153–159.
- PARK, D. S. 1990 The primary and secondary instabilities of Görtler flow. PhD Thesis, University of Southern California.
- STUART, J. T. 1987 A critical review of vortex-breakdown theory. *Vortex Control and Breakdown Behaviour, Second Intl Colloq. on Vortical Flows, Baden, Switzerland*, 6–7 April. 1987.
- TSAI, C.-Y. & WIDNALL, S. E. 1980 Examination of a group-velocity criterion for breakdown of vortex flow in a divergent duct. *Phys. Fluids* **23**, 864–870.
- VINCENT, A. & MENEGUZZI, M. 1991 The spatial structure and statistical properties of homogeneous turbulence. *J. Fluid Mech.* **225**, 1–20.